Vigilada Mineducación

COMPLETION OF INPUT IMAGES OF THE ELASTIC REGISTRATION PROCESS FOR IMRT APPLIED TO BREAST CANCER USING SPLINE-BASED INTERPOLATION

MATEO RIOS QUERUBIN

Tesis de Maestría

Asesor, docente

Juan Carlos Rivera

Henry Laniado

Maria Eugenia Puerta

UNIVERSIDAD EAFIT

Escuela de Ciencias e Ingenierías

Maestría en Matemáticas Aplicadas

Medellín, Antioquia, Colombia

2024

Completion of input images of the elastic registration process for IMRT applied to breast cancer using spline-based interpolation

Mateo Ríos-Querubín (M.R-Q.), Juan Carlos Rivera (J.C.R.),
Henry Laniado (H.L.), Maria Eugenia Puerta (M.E.P.)

School of Applied Sciences and Engineering, Universidad EAFIT,
Medellín, 050022, Antioquia, Colombia.

*Corresponding author(s). E-mail(s): jrivera6@eafit.edu.co;
Contributing authors: mriosqu@eafit.edu.co; hlaniado@eafit.edu.co;
mpuerta@eafit.edu.co;

Abstract

Cancer is one of the leading causes of death worldwide. Radiotherapy plays a fundamental role in its treatment, but the collateral damage of the process can affect patients' quality of life. Intensity-modulated radiation therapy (IMRT) is an advanced technique that offers promising benefits, but input imaging for IMRT incurs high costs. To mitigate collateral damage and increase treatment efficacy, we propose a methodology to expand the input set for IMRT. In this study, we focused on reducing the uncertainty of the data by preprocessing the input images. By employing bootstrapping, a non-parametric statistical sampling technique, we reduce the input images to regions of interest. Interpolating this information using polynomial splines and B-splines generates intermediate images. Our findings show that both interpolation methods, specifically the degree 1 polynomial spline, effectively reduce the uncertainty of the data. The methods are tested using Pearson correlation tests and bootstrap hypothesis tests, finding them accurate. By expanding the input data set and minimizing uncertainty, our approach promises to improve treatment planning and enhance patient outcomes in radiotherapy.

Keywords: Images processing, spline-interpolation, non-parametric statistics, radiation therapy, IMRT

1 Introduction

According to the World Health Organization (WHO) [1], cancer stands as a global scourge, ranking among the leading causes of death worldwide. Nearly 10 million lives were claimed by various types of cancer in 2020, with breast cancer emerging as one of the top five deadliest forms in recent years. In Colombia, 42,000 deaths among women were attributed to cancer in 2021, with breast cancer accounting for approximately 18% of these cases [2].

Radiotherapy, a common treatment for cancer, employs high-energy radiation to damage cancer cells' DNA, preventing their proliferation, causing tumor shrinkage, and even enabling its elimination, as reported by the Radiological Society of North America (RSNA) and the American College of Radiology (ACR) [3]. Radiation is administered in separate doses, either internally through radiation-containing objects like capsules, or externally using machines that utilize photon, proton, or electron beams to irradiate specific areas of the body [4].

External beam radiation therapy encompasses multiple modalities, all striving to deliver the prescribed dose as accurately as possible while minimizing side effects on surrounding tissues, ensuring they remain below the defined maximum dose [5]. Among these modalities is intensity-modulated radiation therapy (IMRT), which uses advanced technology, such as linear accelerators (LINACs), to manipulate photon and proton radiation beams, precisely targeting the tumor volume.

The IMRT process begins by taking medical images of a patient, usually computed tomography (CT) scans or magnetic resonance images (MRI). These images are used among advanced computer calculations to find the best dose pattern for the tumor shape, also called the treatment plan. LINACs have a device called a multileaf collimator made up of thin leaves of lead that can move independently. They can be adjusted precisely around the treatment area, and the lead sheets can move when the machine rotates around the patient. They shape the beam of radiation toward the tumor as the machine rotates. Each radiation therapy beam is divided into many small beams that vary the radiation intensity, allowing different doses of radiation to be delivered through the tumor [6, 7].

Based on the information above, it is deduced that the effectiveness of therapy relies on the quality of the input information: medical images and their registration (translation to a coordinate system). This input set comprises a small number of images due to factors such as costs, radiation exposure for the patient (in the case of CT), data acquisition time, and processing. Generating CT scans typically takes between 10 to 30 minutes, while MRI tests last about 30 to 60 minutes, potentially longer. In the USA, CT scan costs range from \$300 to over \$6 750, with a mean cost of \$3 275. Similarly, MRI costs range from \$375 to over \$2 850, with a mean cost of \$1 325 [8, 9]. The limited amount or imprecise nature of the data used results in inaccuracies in the treatment plan, potentially leading to higher radiation doses being delivered to surrounding areas. These inaccuracies can be attributed, at least partially, to the limited availability of information.

This paper proposes a methodology to complete a set of input images for the elastic registration process applied to breast cancer radiotherapy using spline-based interpolations improved by a bootstrapping method over the data: the lack of information is amended by generating intermediate images between the original ones: Let be a set of N medical images of equal dimensions, each one composed of $I \times J \times K$ voxels. Use splines to interpolate the curve created by taking the voxel i, j, k from all the images generates intermediate points. Repeat this process for each image coordinate, utilizing the results generated by the splines to create the intermediate images.

This document is structured as follows: In Section 2, a comprehensive overview of the subject is provided, including a brief history of cancer, with a particular focus on breast cancer due to its significant impact in Colombia and worldwide (Section 2.1). The section also covers various treatments, including IMRT, along with alternatives such as interpolation to address its disadvantages. The chronology of interpolation methods, specifically polynomial splines, and B-splines, is briefly narrated (Section 2.1). Details regarding the data used in this article are presented in Section 2.2, and the experiments conducted are described in Section 2.3. Additionally, Section 2.4 presents a statistical method aimed at reducing computational costs and increasing interpolation speed, while Section 2.5 outlines the metrics used to assess the accuracy of the interpolations.

In Section 3, the results obtained from the statistical processes and the interpolations are reported. This section includes a description of Algorithm 1, which performs the statistical process to undersample the information to be interpolated (Section 3.1). The algorithm 2 covers the interpolation of polynomials and the necessary modifications to interpolate using B-splines, (detailed in Section 3.2). The results of the experiments and the associated metrics are presented in Section 3.3.

Finally, the document concludes with Section 4. This section analyzes the obtained results, justifies how the undertaken actions have fulfilled the objectives, compares the metrics results with those found in the literature, and discusses the advantages and disadvantages of the performed procedures. Future work is also proposed.

2 Materials and Methods

2.1 Literature Review

The origin of cancer dates back to antiquity: In 1860, the Edwin Smith Papyrus, a medical record containing the oldest known notation of cancer from around 1600 BC, was discovered. Cancer is the name given to a set of related diseases, consisting of the endless division of some cells in the body and their spread to surrounding tissues. Normally, human cells grow and divide, forming new cells as needed, which as they age or become damaged, die and are replaced by new cells. However, when cancer develops, some cells become increasingly abnormal, old or damaged cells survive, and new unneeded cells are formed. These abnormal cells divide without stopping and form unusual growths called tumors [11].

In the 18th century, Jean Louis Petit and Benjamin Bell carried out treatments based on the removal of tissue, lymph nodes, or parts of muscles. This allowed William Stewart Halsted to develop and perfect (for that time) the mastectomy [12]. At the end of the 19th century, after the discovery of X-rays, radiation-based treatments began. During the following years, several milestones were achieved in this regard [13, 14]. By the 1920s, it was understood that divided doses are better than single doses, as they are more effective against cancer and have fewer side effects [15].

In the time that followed these years, supervoltage X-ray tubes were developed, laying the groundwork for future developments such as LINACs. This device uses microwave technology (similar to that used for radar) to accelerate particles, allowing them to collide with a heavy metal target to produce high-energy X-rays. LINACs were modified and finally adjusted for radiotherapy application [15, 16]. They have been used to treat different types of cancer since their discovery, due in large part to their precision, non-invasiveness, and patient safety [5, 17].

In 2005, IMRT is introduced for the first time. This modality uses computer-controlled linear X-ray accelerators: a multi-leaf collimator (MLC), a device capable of narrowing a beam of particles or waves, made of individual "sheets" of a high atomic number material, which by moving in and out of the path of a radiation beam give it shape and vary its intensity. These beams penetrate the body from different angles, assuring that deliver the closest dose to the prescribed one to the target volume, while the delivered dose to surrounding tissues is less than a maximum threshold dose. To plan the treatment, three-dimensional images of the patient are used, which are obtained by CT or MRI. Along with these images, the dose intensity pattern that best fits the shape of the tumor is computed [6, 18, 23].

The disadvantages of this process include inaccuracies in the application of the radiation or residues of it in places that should not have received it [19]. Examples of this are the effects on the dose if there is not enough precision in the calibration on the blades of the multileaf collimators [20], and the collateral damage caused by the inter-fractional movements that certain organs carry out during radiotherapy, and how the isocenter shift modifies received doses [21]. In addition, it is quite a challenge to adequately measure the data and guarantee the quality of the radiation dose distributions, emphasizing the process metrology [22]. Therefore, the correct use of the necessary implements to support the start-up and quality assurance requirements of an IMRT program is included, increasing the limitations subject to those requirements. With these examples, we evidence multiple possible approaches to the problem and, therefore, multiple solutions can be proposed.

Aiming to improve IMRT, increasing the accuracy of the method and thus reducing collateral damage, multiple procedures have been proposed, including the use of robust optimization to reduce uncertainties caused by inter-fractional motions [26], and image interpolation using splines, either to improve the quality of an image or generating new images. The latter can be applied to three-dimensional images using B-splines and voxel-by-voxel interpolation [27]. It is also possible to take an input set for broader treatment plans, by taking more images or using procedures such as four-dimensional computed tomography (4DCT). However, these procedures have high time, money, and radiation, so solutions based on image interpolation or robust optimization are more prudent approaches to solve the problem.

Let us focus on the interpolation processes. From 1633, the works on interpolation begin to be formalized in mathematical terms and their uses begin to expand. In 1670, Gregory [35] described the Gregory-Newton interpolation formula for data of equal intervals, so named because Newton in his Lemma V of Book III of Philosophiae

Naturalis Principia Mathematica (1687), in which the general interpolation formula for unequal-interval and equal-interval data are described, the latter being a special case of the former and is the same as described by Gregory. Later, in 1821, Cauchy [32] studies the interpolation due to two polynomials and shows that the solution to this problem is unique.

Later, in 1885, Weierstrass [36] proves the approximation theorem, which states that every continuous function on a closed interval can be uniformly approximated to any precision prescribed by a polynomial, justifying the use of polynomials for the approximation of functions. However, later it would be known that this theorem does not necessarily hold. In 1906 Birkhoff [37] defined a general interpolation problem: Given any set of points, find a polynomial function that satisfies the given criteria on its value and/or the value of any of its derivatives for each individual point.

In 1946, Schoenberg [33] shows that any of the then-existing polynomial interpolation formulas can be written as a linear combination of shifted versions of some basic function, which completely determines the properties of the resulting interpolation. Furthermore, he introduces the notion of a mathematical spline: a differentiable curve defined in portions by polynomials (frequently used in interpolation problems due to their simplicity of representation and their ease of computation, commonly defined for interpolation as minimizers of the appropriate roughness measurements subject to a series of restrictions [24]). The simplest type of splines are the polynomial ones, which are nothing more than piecewise polynomial functions, defined as follows:

Let S be a function that takes values from the interval $[a, b]$ and maps them to $\mathbb{R}$, as shown in Equation (1).

$$S : [a, b] \to \mathbb{R} \tag{1}$$

As it is meant to be piecewise, the interval $[a, b]$ must be split in η ordered sub-intervals with pairwise disjoint interiors. Consider now, η values $t_i \in [a, b]$, $i = 0, \ldots, \eta - 1$, such that $a = t_0 < t_1 < \cdots < t_{\eta-1} < t_\eta = b$, then:

$$[a, b] = \bigcup_{i=0}^{\eta-1} [t_i, t_{i+1}] \tag{2}$$

Therefore, polynomials $P_i : [t_i, t_{i+1}] \to \mathbb{R}$ of degree n are defined in Equation (3).

$$S(t) = P_i(t) = \sum_{j=0}^{n} \beta_{ij} (t - t_i)^j \qquad \forall\, t \in [t_i, t_{i+1}] \tag{3}$$

About 20 years later, Schoenberg [25] introduced the term B-splines as spline functions that have minimal support with respect to a certain degree, smoothness and partition of the domain. Any spline curve can be written as a linear combination of B-splines, as long as they comply with the same characteristics of domain, degree, smoothness and partition. These kind of splines are proved to be superior over other popular approaches such as nearest-neighbor, linear, or windowed-sinc by Hou & Andrews in 1978 [38]. Schoenberg's findings found utility in approximation theory, numerical analysis, statistics, geometric modeling, computer-aided geometric design, and computer graphics.

Between 1948 and 1949 Shannon [34], referring to the works of J. M. Whittaker and Nyquist, presents and proves the sampling theorem, whose solution has applications in fields such as communications engineering, signal processing and analysis applications and, to a certain extent, in numerical analysis.

2.2 Data Description

In general, medical images used to create IMRT plans are CT scans or MRI. Those images are recorded in DICOM (Digital Imaging and Communications in Medicine) image format, created by the National Electrical Manufacturers Association (NEMA) as the standard for the distribution and display of medical images. The content of these files may include other details, such as the name of the patient and the date of the study. Anonymized data is provided by matRad, a treatment planning system created at the German Cancer Research Center (DKFZ) for academic purposes, featuring functions and classes that simulate the complete treatment planning workflow.

For this study, a data set of N consecutive images is used, whose pixel array (the information matrix of the DICOM images that contain the data that represents the image) of $I \times J \times K$ voxels, where $N=4$, $I=512$, $J=512$ and $K=75$. These images represent 4 moments of a torso with breast cancer, each separated into 75 slices of 512×512 pixels (or $512 \times 512 \times 75$ voxels). Each of these slices is composed of a black section that surrounds the organ which is equivalent to about half of the image information, and a gray-toned section that contains data of organs. An example of some slices of some images lies in Figure 1.

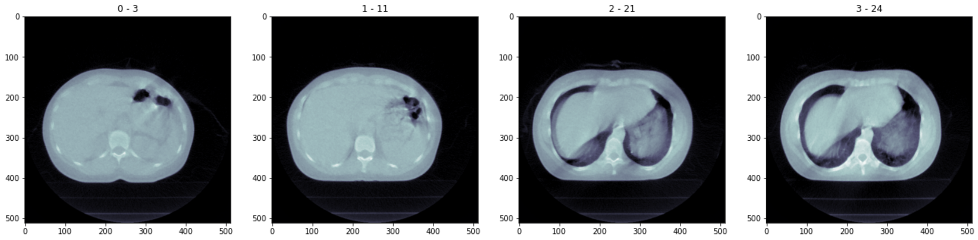

(a) Slice 3 from image 1

(b) Slice 11 from image 2

(c) Slice 21 from image 3

(d) Slice 24 from image 4

Fig. 1: Different slices from different images.

2.3 Experiments

Generating treatment plans for IMRT requires sequential medical images. In order to create new images that represent the values between the original ones, we interpolate these sequential images. For this, interpolation methods using polynomial splines and B-splines, of degrees 1, 2, and 3, are proposed. In addition to applying these methods, in order to evaluate their performance two sets of experiments are proposed.

The first experiment consists of using polynomial splines and B-splines of degrees 1, 2, and 3 to generate new images from the data set described in the data section, in order to verify their ability to create new images from the original ones.

In the second experiment, we select a subset (Q_m) composed of non-consecutive images of the original data (Q), separated by intermediate images over the dimension of K, i.e. if a first index is q, the next ones are $q+2,\ q+4,\dots$ This subset size is less than half the data ($|Q_m| < |Q|/2$, where $|\bullet|$ measures the amount of data in the set $\bullet$). Submit this set to the interpolation methods and evaluate their results by comparing the new images with the original ones using error metrics: *Dice coefficient*, *Pearson's correlation coefficient* and a *process Bootstrapping* (these metrics are explained in detail in Section 2.5).

Each one of the images described in Section 2.2 has 75 two-dimensional slices, on which it is possible to extract Q_m, as defined, interpolate and calculate metrics. This should not affect the results since the three-dimensional images are decomposed to their points and it is on these that the interpolation is calculated, the same as it would be done on the two-dimensional images, so in both cases what is measured is the precision of interpolating the points. Therefore, the calculations on 3 dimensions are a calculation on the results of 2 dimensions on which the quality does depend.

A concise demonstration will be performed to substantiate this: Having $D_{pa} = [d_{ijkn}]$, a four dimensional matrix (detailed in section 3.1), every error metric we are using (E) is applied to vectors $d_{ijk} = [d_{ijk1},\ d_{ijk2},\ \dots,\ d_{ijk(n-1)},\ d_{ijkn}]$, producing $E(d_{ijk})$. Calculating the metric for the whole set would be equal to the average over the three dimensions (represented by indexes i, j, and k):

$$\frac{1}{KJI}\sum_{k=1}^{K}\sum_{j=1}^{J}\sum_{i=1}^{I}E(d_{ijk}) = \frac{1}{K}\sum_{k=1}^{K}\left(\frac{1}{JI}\sum_{j=1}^{J}\sum_{i=1}^{I}E(d_{ijk})\right) \tag{4}$$

which represents the calculus of the metric for every slice k and then finds the result for the whole set averaging the values of k. This justifies that the proposed procedure is equivalent.

2.4 Undersampling

As mentioned in Section 2.2, the set of images has a dimension of $I \times J \times K \times N$, that is, $N = 4$ images of $I \times J \times K = 512 \times 512 \times 75$ voxels. The methods used to generate the interpolations require a high amount of memory (between 1.89 Gb and 2.63 Gb approximately for each interpolation), for which an undersampling process is proposed. Its memory expense is such small that it is negligible; it takes 0.38 seconds to execute, and it is capable of reducing the necessary physical memory resources of each interpolation to less than 1 Gb (between 0.63 Gb and 0.81 Gb approximately). Then, using this method the memory consumption is reduced at least by more than 1 Gb, and execution time to less than half of the time it used to take.

Consider, in the first place, that the images used are composed in a proportion of voxels that contain information about the body with respect to the voxels that do not (they are black voxels) of approximately 1:1, 1 contains, 1 does not; this proportion can vary but very subtly. Making interpolations over the complete images implies processing more information than is necessary since it is only desirable to interpolate the gray voxels.

Given this, we propose to separate the black voxels from the gray ones and interpolate only the latter. To do so, we must take into account that each slice of our images is a matrix of intensities that can be represented as a scatter plot. Each image is composed of 75 slices, thus, it is feasible, to apply the law of large numbers to functional data, to obtain an estimate of the expected scatter plot. This estimate is generated by computing the mean of the slices from each image. After calculating this, find the percentiles that are multiples of 5 for this expected curve, and call them q_t, $t \in \{0, 5, 10, 15, \ldots, 90, 95\}$. The differences between these percentiles are found as the subtraction between the next percentile and the current one, generating the variables $d_t = q_{t+\Delta} - q_t$; where Δ can be any value between one percentile and the next, but it is suggested to use 5 to keep the experiment cohesive and produce the desired results. Calculate the mean of the differences as $(\overline{d})$ and find q_t such that $d_t > \overline{d}$. Repeat this process for multiple images and keep the minimum between them by calling it q_t^s.

Figure 2 (a) shows the scatter plot of the expected behavior of the values of the voxels of image $N = 4$, obtained by averaging all its K slices. On the other hand, in Figure 2 (b) lies its ordered version along with its percentiles. Designate them as Px, where x is the corresponding percentile, for instance, P60 for percentile 60. It is seen that changes between the values of P start getting bigger after $P45$. Doing the calculations explained before, it its the breaking point. This point also reflects one of the last points before a significant change in slope, which happens just before the end of the points without information.

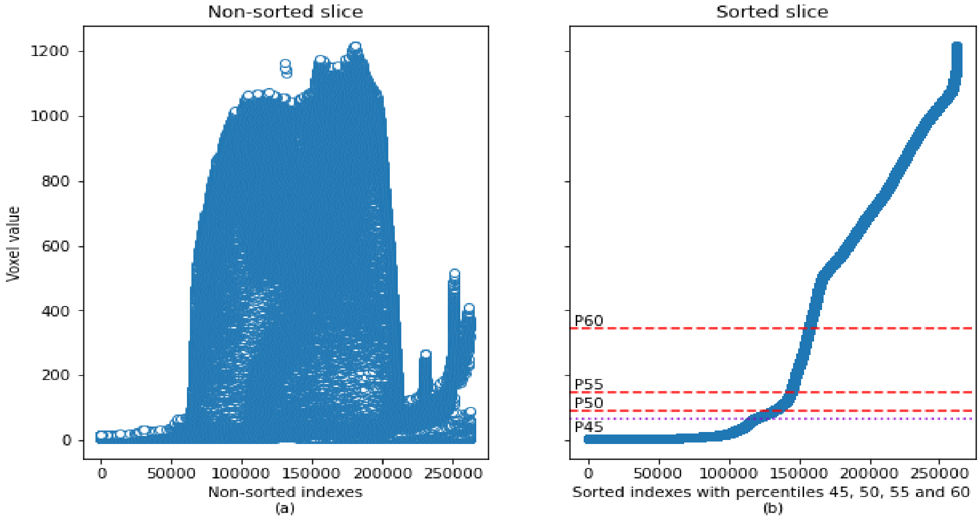

Fig. 2: Non-sorted and sorted scatter for the expected behavior of the voxels values for $N = 4$

Thus, it is decided to keep the points such that the value of the voxel i, j, k is greater than q_t^s. It is also clarified that this procedure was carried out with more values of Δ but the one that best captures the changes in inclination of the curve was 5.

2.5 Metrics

Let us call Q the original set of data after applying it to the undersampling process described in Section 2.4. A sample Q_m is taken, as described in Section 2.3, on which the different interpolation processes presented in this document are applied, generating the set $\hat{Q}_m$. The following metrics are proposed to measure the proficiency of these interpolations.

1. Dice coefficient: Also known as the Sørensen–Dice index, it is a statistic that measures the similarity between two sets [28], using Equation (5).

   $$Dice(Q_m, \hat{Q}_m) = \frac{2|Q_m \cap \hat{Q}_m|}{|Q_m| + |\hat{Q}_m|} \tag{5}$$

   As $| \bullet |$ is the cardinal of the set $\bullet$, and both sets have the same size in our experiments, Equation (5) can be reduced to Equation (6).

   $$Dice(Q_m, \hat{Q}_m) = \frac{|Q_m \cap \hat{Q}_m|}{|Q_m|} \tag{6}$$

   Since these sets are actually data matrices, we decided to measure the cardinal of the interpolation of two items ($|\bullet \cap \circ|$) as 1 if the difference between them is lower than a threshold and 0 otherwise. Then, the cardinal of the interpolation of both sets ($|Q_m \cap \hat{Q}_m|$) is considered the number of values that, when subtracted from each other, are zero under a tolerance τ. Note that if Q_m and $\hat{Q}_m$ are equal, the coefficient is equal to 1, which means a perfect prediction, and making it desirable to have values close to 1. On the other hand, if the coefficient becomes 0 it means that all the predictions are wrong, so lower values become undesirable.
2. Pearson's correlation coefficient: It is a measure of linear dependence between two quantitative random variables, which is responsible for measuring the degree of relationship of two variables as long as both are quantitative and continuous as described in Equation (7).

   $$\rho(Q_m, \hat{Q}_m) = \frac{\sum((Q_m - \overline{Q_m})(\hat{Q}_m - \overline{\hat{Q}_m}))}{\sqrt{\sum(Q_m - \overline{Q_m})^2 \sum(\hat{Q}_m - \overline{\hat{Q}_m})^2}}, \tag{7}$$

   where $\overline{Q_m}$ and $\overline{\hat{Q}_m}$ correspond to the means of sets Q_m and $\hat{Q}_m$ respectively, and $\sum \bullet$ indicates the sum over all the indices of $\bullet$. This metric allows us to recognize the similarity between two curves except for a scale factor, with values between -1 and 1. Here, values closer to 1 or -1 represent high similarity or dependence (positive or negative), while values closer to 0 represent low similarity or dependence.
3. Bootstrapping: using bootstrapping as a significance test for the difference between two populations consists of:

(a) Exchange between both groups a fixed amount of randomly selected values, generating two mixed samples. Assign them the labels Q_m^M and $\hat{Q}_m^M$, where Q_m^M is made up of 95% Q_m values and 5% $\hat{Q}_m$ values, and Q_m^M is made up of 95% $\hat{Q}_m$ values and 5% Q_m values.

(b) Apply a t-test over the to mixed samples, Q_m and $\hat{Q}_m$. It is a test for the null hypothesis that 2 independent samples have identical expected values, assuming that both of them have identical variances.

(c) Repeat the two previous steps multiple times generating the distribution of the expected values.

(d) With the curve centered in 0, count the points at the left of $-\alpha/2$, being it p^-, and the points at the right of $\alpha/2$, being it p^+, with $\alpha = 95\%$. Then, calculate the two-tailed p-value as 2 times the minimum between them: $p - value = 2\ min\{p^-, p^+\}$.

This procedure provides information about the similarity of the data without excluding a scale factor, returning a p-value that represents if the data is equal or not. Let us call the result of each individual curve q, b_q, equal to 1 if the test concludes that equality of means is not rejected, 0 otherwise.

Interpolations are calculated over Q_m, which has dimensions $I_q \times J_q \times K_m$, having $I_q < I$, I_q: number of values regarding i after the undersampling process, $J_q < J$, J_q: number of values regarding j after the undersampling process, and $K_m < K$, K_m: number of samples taken. This results in $I_q \times J_q$ interpolated curves, q, of K_m values, whose b_q values are averaged to obtain the result of this test.

3 Results

In this section, three experiments are performed in order to evaluate the proposed methodology. In Section 3.1 is evidenced the bootstrapping results that reduce the magnitude of the data to be processed. Then, the results of the interpolations such as the pseudocodes, and the details of the developed methods are described in Section 3.2. Finally, Section 3.3 shows the results of the experiments proposed in Section 2.3.

3.1 Undersampling Procedure

The first result is the method in charge of separating the gray voxels from the black ones, represented in Algorithm 1. This process is based on the expected distribution of the data and the differences in their percentiles for the indices corresponding to each group of voxels, and thus only interpolates those with useful information. Consider that, for each image n of N, we have K slices of similar behavior, which can be represented by their average in view of their similarity and the amount of data per image. Taking this expected dispersion of points, extracting from it certain percentiles separated by a value Δ, and finding the differences between them, it is possible to find a value that represents where the ordered curve of points changes its slope, which means when the black dots end and the gray ones begin.

This algorithm receives a matrix of pixels D_{pa} of dimensions $I \times J \times K \times N$ and a value (Δ) with which the point at which the change of the slope of the ascending-ordered expected scatter plots is larger (as explained in Section 2.4. First, set n equal to 1 as the iterator over the images of N, and ls as an empty list which then contains the percentages that meet the conditions described in Section 2.4 for finding the breakpoint q_t^s.

Thus, iterating n from 1 to N, data of pixel array of image n is stored at D_{pan}, and its mean over dimension K is calculated to obtain the expected behavior of the scatter of points, D_m. Then, $1/\Delta$ percentiles of D_m are found and kept in lq_t, and the differences between each consecutive pair of them are stored in ld_t. The mean of differences ld_m is used to calculate the maximum percentile lower than ld_m, stored in ls. Then, the minimum of the ls is selected as the threshold that defines the indexes that belong to each group the voxels with the most representative information of the images, and those that do not).

Finally, a dictionary is defined as $index\_dic \leftarrow create\_index\_dictionary()$, containing the ordered indices and the original voxels to which they correspond (for instance, index 130 can correspond to voxel $(5, 18)$). Using this dictionary and the threshold found (q_t^s), a list LV of voxels corresponding to the organized indices after the cut q_t^s is built. The list LV corresponds to the voxels having the most representative information of images and they are the voxels that the proposed interpolation methods use to generate new images.

Algorithm 1 Selection of the most representative data

```
Require: $D_{pa}$, $\Delta$
$n, ls \leftarrow assign\_initial\_values()$
while $n \leq N$ do
    $D_{pan} \leftarrow D_{pa}[n]$
    $D_m \leftarrow mean\_over\_k(D_{pan})$
    $lq_t \leftarrow get\_percents(D_m, \Delta)$
    $ld_t \leftarrow calculate\_differences(lq_t)$
    $ld_m \leftarrow mean(ld_t)$
    $ls \leftarrow update\_with\_q_t\_fulfills(lq_t, ld_t, ld_{mean})$
end while
$q_t^s = min(ls)$
$index\_dic \leftarrow create\_index\_dictionary()$
$index\_new \leftarrow select\_indexes(index\_dic, q_t^s)$
return $index\_new$
```

This procedure makes it faster to process images of this type since it reduces the amount of data to be processed in a category of images in which it does not seem feasible to generate a convex covering (a solution that would be practical and ideal).

3.2 Interpolation Procedures

The pseudocode that represents the interpolation method for polynomial splines is depicted in Algorithm 2, which can be modified to represent B-splines procedures; the required adaptation is presented later in this section. Given a set of images, a desired spline degree, and a list of indices to be processed, the procedure generates polynomial splines for each sequential set of voxels (i.e. the vector of size $N \times 1$ generated for each voxel i, j, k of each image). From these splines it generates intermediate points that build, as these are generated, the intermediate images. Note that, when input voxels are reduced by using Algorithm 1, the computational effort is also reduced in Algorithm 2.

This algorithm starts extracting the shape of the pixel array D_{pa} into constants I, J, K and N and generating two vectors: x, a vector of integers from 1 to N, and x_new, a vector of $2N-1$ values from 1 to N with step 0.5, i.e. $x\_new = [1.0, 1.5, 2.0, 2.5, \ldots, N-0.5, N]$. Then, a matrix D_{bgt} of dimensions $(I \times J \times K \times 2N{-}1)$ is generated to store the results of the interpolations process. The interpolations are stored in $D_{bgt}(n)$, assigning the original images at the odd indices and the interpolated images at the even indices; in this way, between each pair of original images there is an interpolated one. As described in Sections 2.4 and 3.1, the amount of data to be interpolated is reduced through the mentioned bootstrapping process finding the points with valuable information. Therefore, to reduce the computational effort, the creation of D_{bgt} includes assigning the original images in their respective positions, at the odd values of n, and setting the non-interpolable points for all images (for instance, black voxels must have all very similar values).

Then k is initialized to iterate from 1 to K, representing the slices of the images. For each slice, the counter p is initialized, which iterates over the number of points selected from Algorithm 1, $points\_from\_index\_new$. The coordinates i and j are extracted from the point $points\_from\_index\_new$ in p and the vector y is generated with the values of the voxels i, j, k for each one of the N images, i.e. $y = [D_{pa}[i,j,k,1],\ D_{pa}[i,j,k,2],\ \ldots,\ D_{pa}[i,j,k,N-1],\ D_{pa}[i,j,k,N]]$. From the vectors, x and y, and the degree g, a polynomial spline ($polynomial\_spline$) is generated. Computing the values of this spline for the vector x_new produces y_new, which contains the values of the interpolations for the coordinates i, j, k. These values are assigned to their respective places on D_{bgt} and p is updated. This process is repeated until all the points are calculated for slice k. Then k is updated to calculate the values for the following slice. When this process ends, D_{bgt} contains both the original and interpolated images.

As mentioned before, Algorithm 2 can be modified to apply B-splines to generate interpolations. The resulting B-spline-based algorithm can be obtained by replacing `line 12` using the following commands:

```
$bspline \leftarrow generate\_bspline(polynomial\_spline)$
$y\_new \leftarrow interpolate(x\_new, bspline)$
```

where $generate\_bspline(polynomial\_spline)$ creates a univariate spline on the B-spline basis, from a polynomial spline; and $interpolate(x\_new, polynomial\_spline)$ generates the interpolation results for the points x_new and B-spline $bspline$.

The resulting algorithm generates B-splines for each sequential set of voxels, using the images, the desired spline degree, and the indices reduced from the data reduction process. From these splines it generates intermediate points that build, as these are generated, the intermediate images.

Algorithm 2 Interpolate polynomial splines

```
**Require:** $D_{pa}$, $g$, $points\_from\_index\_new$
$I,\ J,\ K,\ N \leftarrow get\_shape(D_{pa})$
$x \leftarrow generate\_int\_array(N)$
$x\_new \leftarrow generate\_array(N, step = 0.5)$
$D_{bgt} \leftarrow duplicate\_to\_intermediates(D_{pa})$
$k \leftarrow initialize()$
while $k \leq K$ do
    $p \leftarrow initialize()$
    while $p \leq size(points\_from\_index\_new)$ do
        $i,\ j \leftarrow points\_from\_index\_new[p]$
        $y \leftarrow D_{pa}[i, j, k]$
        $polynomial\_spline \leftarrow get\_polynomial\_spline(x, y, g)$
        $y\_new \leftarrow interpolate(x\_new, polynomial\_spline)$
        $D_{bgt}[i, j, k] \leftarrow y\_new$
        $p \leftarrow p + 1$
    end while
    $k \leftarrow k + 1$
end while
```

Despite being an expansion of the interpolation methods found in scipy, these procedures find utility in the possibility of interpolating this type of image efficiently when combined with the size reduction method. In addition, the algorithms generated by being able to produce the desired interpolations increase the amount of data available, improving the quality of the input set.

3.3 Experimental Results

The numerical results corresponding to the experiments proposed in Section 2.3 are presented in this section. First, to test how the interpolation methods work, Figures 3, 4 and 5 show original and interpolated slices of different images using polynomial interpolation.

Likewise Figures 6, 7 and 8 reflect original and interpolated slices of different images using the B-spline interpolation method.

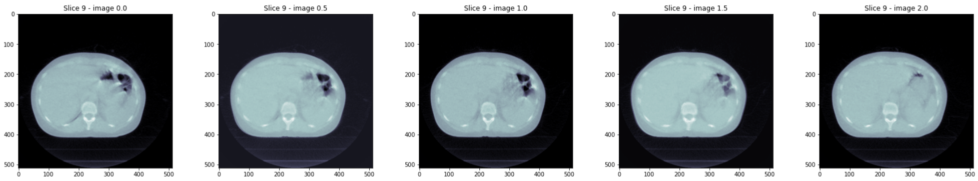

(a) Slice 9 from image 1
(b) Slice 9 from image 1.5
(c) Slice 9 from image 2
(d) Slice 9 from image 2.5
(e) Slice 9 from image 3

Fig. 4: Slice 9 of the original images 1, 2 and 3, and its interpolation using the polynomial spline method of grade 2, generating images 1.5 and 2.5.

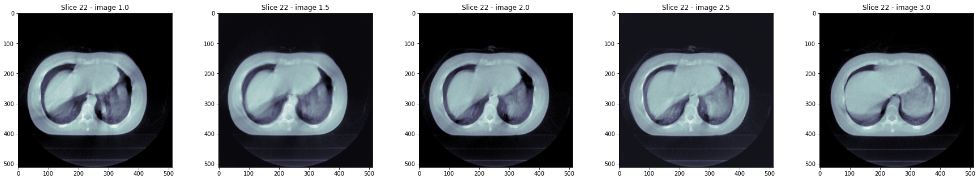

(a) Slice 22 from image 2
(b) Slice 22 from image 2.5
(c) Slice 22 from image 3
(d) Slice 22 from image 3.5
(e) Slice 22 from image 4

Fig. 5: Slice 22 of the original images 2, 3 and 4, and its interpolation using the polynomial spline method of grade 3, generating images 2.5 and 3.5.

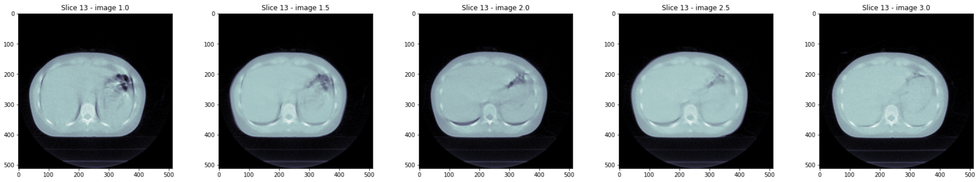

(a) Slice 13 from image 2
(b) Slice 13 from image 2.5
(c) Slice 13 from image 3
(d) Slice 13 from image 3.5
(e) Slice 13 from image 4

Fig. 3: Slice 13 of the original images 2, 3 and 4, and its interpolation using the polynomial spline method of grade 1, generating images 2.5 and 3.5.

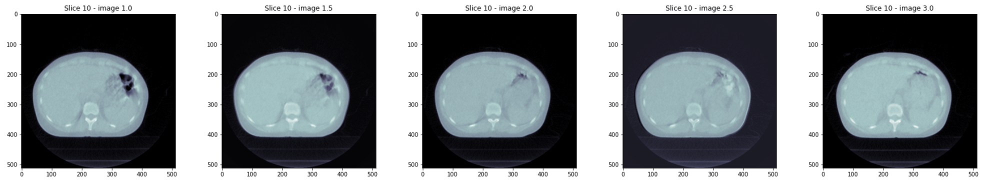

(a) Slice 10 from image 2 (b) Slice 10 from image 2.5 (c) Slice 10 from image 3 (d) Slice 10 from image 3.5 (e) Slice 10 from image 4

Fig. 8: Slice 10 of the original images 2, 3, and 4, and its interpolation using the B-spline method of grade 3, generating images 2.5 and 3.5.

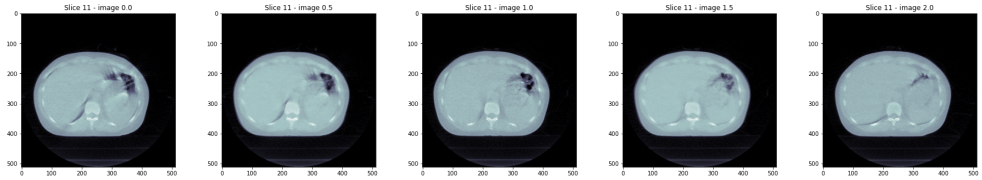

(a) Slice 11 from image 1 (b) Slice 11 from image 1.5 (c) Slice 11 from image 2 (d) Slice 11 from image 2.5 (e) Slice 11 from image 3

Fig. 6: Slice 11 of the original images 1, 2 and 3, and its interpolation using the B-spline method of grade 1, generating images 1.5 and 2.5.

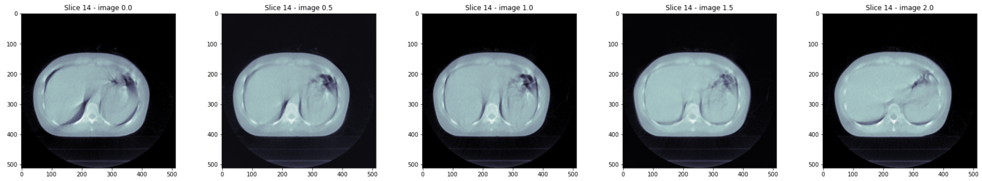

(a) Slice 14 from image 1 (b) Slice 14 from image 1.5 (c) Slice 14 from image 2 (d) Slice 14 from image 2.5 (e) Slice 14 from image 3

Fig. 7: Slice 14 of the original images 1, 2, and 3, and its interpolation using the B-spline method of grade 2, generating images 1.5 and 2.5.

Table 1 records the numerical results in terms of computing times and different statistical methods. Columns correspond to the six different interpolation methods: the first three are polynomial splines with degrees 1, 2, and 3, and the last ones are B-splines with the same degrees. For each method, the second row indicates the computing time required to execute each procedure in a computer Acer Nitro

AN515-55 with Microsoft Windows 11, Intel(R) Core(TM) i5-10300H CPU 2.5Ghz. Rows three, four, and five contain the results of Dice, Pearson, and Bootstrap metrics, exposed in Section 2.5, applied to the interpolation methods stated in Section 2.3.

To accomplish this, 19 consecutive slices, which represent approximately 25% of the total slices, will be randomly selected from each of the four images using the same set of indices. Let us denote these selected slices as K_m. The intermediate cuts are extracted from each set K_m (for instance, if the slices go from 1 to 19, slices 2, 4, 6, ..., 18 are extracted) generating a new set of size 10 which we submit to the different interpolation methods, which fill in the intermediate values to generate the sets K_{me}, each of size 19.

We then proceed to compare the sets K_{me} with their original K_m using the Dice, Pearson, and Bootstrap metrics. These metrics are averaged for the set of images according to Equation (8):

$$average\_metric = \sum_{n=1}^{N} metric(K_m[n], K_{me}[n]), \tag{8}$$

where $K_m[n]$ represents the sample taken from image n and the average metrics, which are shown in Table 1, are the average value of the metrics in each sample of the images.

We then find that the results of the Pearson metrics and bootstrap tests are quite good. These are very close to one, showing that the methods are capable of accurately representing intermediate images.

Table 1: Execution time (in minutes) and metric values of polynomial and B-spline interpolations of grades 1, 2, and 3.

	Polynomial splines			B-splines		
Grades	1	2	3	1	2	3
Minutes	2.65	2.68	2.76	15.8	16.37	16.26
Dice	0.7107	0.7066	0.7013	0.7069	0.7035	0.6983
Pearson	0.9994	0.9995	0.9995	0.9994	0.9994	0.9994
Bootstrap	0.9814	0.9747	0.9702	0.9755	0.9689	0.9631

4 Discussion

The objective of this article is to establish interpolation methodologies based on splines and B-splines polynomials, capable of generating intermediate images for sets composed of MRI or CT (such as those used in IMRT), in such a way that the lack of information on these data is reduced. Achieving this is an important contribution because without taking more images, avoiding the implications exposed in Sections 1 and 2, we can expand the registry by creating new images properly, which could generate more exact treatment plans. In addition, due to the way in which the methods were established, contributes to the treatment of this type of image in a faster way using non-parametric statistics, finding an analog of the convex coating for them.

We introduce in Section 3.2 the pseudocodes that represent the interpolation method developed in Python in charge of generating the polynomial spline and B-spline interpolations for the data sets. Results of these interpolations can be found in Section 3.3, where the results of the proposed experiments (Section 2.3) were described and a good performance is visually appreciated. In these results it is possible to notice that the methods work, creating the intermediate images that were intended to be generated.

The good performance of these results is also evidenced by the metrics proposed in Section 2.5, whose results are found in Table 1. These expose the execution times of the methods using the specified equipment and the values of the different used metrics.

We will commence with the evaluation of the execution time. Let us emphasize that a CT scan usually takes between 10 and 30 minutes to perform, just as an MRI usually takes between 30 and 60 minutes to generate a not very high number of images. Note that the maximum time it takes for the B-splines to generate their results, 16 minutes, is slightly greater than the minimum time it takes to perform a CT scan and allows us to generate enough images to have almost double the ones obtained in the CT. We then get a larger and more detailed set for a low amount of time, much lower when compared to the time of an MRI. Focusing on polynomial splines, the picture is even better because the maximum time they take to compute, 2.7 minutes, is just one forth of the minimum time for a CT and one tenth of the minimum for an MRI. Speaking only in terms of time, both type of methods are efficient, especially the ones based on polynomial splines.

Due to the statistical process defined in Section 2.4 applied over the data by means of the algorithm described in Section 3.1, these methods can have a shorter computing time than a simple interpolation. This procedure reduced execution times by about half (Section 2.4) and reduced the computational cost of resources (CPU and RAM usage) by a similar magnitude, finding it quite useful when dealing with images of this type that have sections without relevant information.

We will now delve into the comparison of metrics for different methods. For the three proposed metrics, both type of methods performed quite well. We found competitive results in the modified DICE metric, a little higher than 0.7, also discovering that the modifications made to said method make it very susceptible to the τ tolerance defined in Section 2.5. For the Pearson and Bootstrapping metrics, the results were very good. For Bootstrapping, all the methods exceeded a similarity of 0.963, reaching a maximum value of 0.981, evidencing high precision of the methods, since when exchanging real records for interpolated ones, no major differences were found, especially for those results obtained from polynomial splines. Every Pearson coefficient exceeded 0.999, showing great linear dependency between the interpolations and the real images for both cases, since the difference between polynomial splines and B-splines is barely notable in this metric. If metrics are also used as a decision criterion to perform these interpolations, it is strongly suggested to use the polynomial splines, recommended above all the one of degree 2, because within this group, which already presents better results in time and metrics than the B-splines, is the one that performs the best. It is important to clarify that the Pearson result combined with

Bootstrap suggests a result of equality; since it reflects a high similarity both in form and magnitude.

In the literature it is possible to find different approaches to track the change and reduce the uncertainty raised, such as tracking the propagation of logarithmic elastic contours and heuristics as shown in [29]. There, through Pearson's correlation, efficient results higher than 0.90 are also found, showing that said approximation to the problem is considerably good, and using an unmodified DICE metric, they find consistent results with what Pearson found. DICE metric is not comparable with the modified DICE metric, since it would be inconsistent due to the adaptations made to it, and even so, both versions are consistent with what is shown by their accompanying metrics. These results allow us to affirm that both methods are quite appropriate as approaches to improve IMRT data and potentially improve the said procedure. Furthermore, it was found that the modified DICE metric, as mentioned above, is susceptible to the chosen tolerance. Even so, the developed methods were achieved with promising results, both in metrics and in time.

To conclude, it is proposed as future work to find sufficient information about radiation and collateral damage that would be partially avoided by generating more images using the proposed methods. In addition, it is proposed to use the interpolated images to calculate treatment plans by means of robust optimization methods and compare the results with the use of the original images.

Declarations

4.1 Funding

"This research was funded by the Ministry of Science, Technology and Innovation (MinCiencias) of Colombia, the El Rosario Clinic, and the EAFIT University, through the agreement with code: 121677757715."

4.2 Conflict of interest/Competing interests

"The authors declare no conflict of interest". "The funders had no role in the design of the study; in the collection, analyses, or interpretation of data; in the writing of the manuscript, or in the decision to publish the results".

4.3 Ethics approval

"Not applicable".

4.4 Consent to participate

"Not applicable".

4.5 Consent for publication

"Not applicable".

4.6 Availability of data and materials

The data used in this manuscript was provided for the development of this research and not propagated by members of the MatRad software development team (https://e0404.github.io/matRad/). If you wish to access said data, you should check with the researchers of this document if your request complies with the information disclosure policies of said software.

4.7 Code availability

"Not applicable".

4.8 Authors' contributions

Conceptualization, H.L, J.C.R., M.E.P. and M.R.; methodology, H.L, J.C.R., M.E.P. and M.R.; software, M.R.; validation, H.L, J.C.R., M.E.P. and M.R.; formal analysis, H.L, J.C.R., M.E.P. and M.R.; investigation, H.L, J.C.R., M.E.P. and M.R.; resources, J.C.R., M.E.P. and M.R.; data curation, M.R.; writing—original draft preparation, J.C.R. and M.R.; writing—review and editing, H.L, J.C.R., M.E.P. and M.R.; visualization, M.R.; supervision, H.L, J.C.R., M.E.P. and M.R.; project administration, H.L, J.C.R., M.E.P. and M.R.; funding acquisition, M.E.P. and J.C.R. All authors have read and agreed to the published version of the manuscript.

Appendix A Abbreviations

The following abbreviations are used in this manuscript:

3D-CRT	3D conformal radiotherapy
4DCT	four-dimensional computed tomography
ACR	American College of Radiology
CT	Computed Tomography
DNA	deoxyribonucleic acid
DICOM	Digital Imaging and Communications in Medicine
IMRT	Intensity Modulated Radiation Therapy
LINAC	Linear accelerators
MLC	Multi-leaf collimator
MRI	Magnetic Resonance Imaging
NEMA	National Electrical Manufacturers Association
RSNA	Radiological Society of North America
WHO	World Health Organization

References

[1] Cancer. Available online: https://www.who.int/news-room/fact-sheets/detail/cancer.

[2] Incidencia del cáncer se redujo en los últimos 3 años. Available online: https://www.minsalud.gov.co/Paginas/Incidencia-del-cancer-se-redujo-en-los-ultimos-3-anos.aspx

[3] Radiation Therapy (Oncology). Available online: https://www.radiologyinfo.org/en/onco.

[4] Radiation Therapy to Treat Cancer. Available online: https://www.cancer.gov/about-cancer/treatment/types/radiation-therapy.

[5] External Beam Radiation Therapy for Cancer. Available online: https://www.cancer.gov/about-cancer/treatment/types/radiation-therapy/external-beam

[6] Sola, A. Radioterapia de intensidad modulada (IMRT). *Revista Médica Clínica Las Condes* **2011**, *22*, 834–843.

[7] Intensity modulated radiotherapy. Available online: https://www.cancerresearchuk.org/about-cancer/cancer-in-general/treatment/radiotherapy/external/types/intensity-modulated-radiotherapy-imrt.

[8] CT Scan for Cancer. Available online: https://www.cancer.org/treatment/understanding-your-diagnosis/tests/ct-scan-for- cancer.html.

[9] MRI. Available online: https://medlineplus.gov/ency/article/003335.htm.

[10] A Brief History of Breast Cancer. Available online: https://www.healthcentral.com/slideshow/a-brief-history-of-breast-cancer.

[11] What Is Cancer?. Available online: https://www.cancer.gov/about-cancer/understanding/what-is-cancer.

[12] Cameron J. L. Our Surgical Heritage. *Ann Surg* **1997**, *225(5)*, 445–458.

[13] Rontgen W. C. Über eine neue Art von Strahlen. *Ann Phys* **1898**, *300*, 12–17.

[14] Grubbé E. H. Priority in the therapeutic use of X-rays. *Radiology* **1933**, *21(2)*, 156–162.

[15] Coutard H. Principles of X-ray therapy of malignant disease. *Lancet* **1934**, *224*, 1–4.

[16] Dutta, S. and Woo, R. and Krummel, T. Advanced and Emerging Surgical Technologies and the Process of Innovation. *Pediatric Surgery* **2012**, *1*, 37–75.

[17] Balagamwala, E. and Stockham, A. and Macklis, R. and Singh, A. Introduction to Radiotherapy and Standard Teletherapy Techniques. *Dev Ophthalmol* **2013**, *52*, 1–14.

[18] Intensity-modulated radiation therapy (IMRT). Available online: https://www.mayoclinic.org/tests-procedures/intensity-modulated-radiation-therapy/about/pac-20385147.

[19] Lee, TF and Sung, KC and Chao, PJ and Huang, YJ and Lan, JH and Wu, HY and Chang, L and Ting, HM. Relationships among patient characteristics, irradiation treatment planning parameters, and treatment toxicity of acute radiation dermatitis after breast hybrid intensity modulation radiation therapy. *PLoS One* **2018**, *13(7).*

[20] Sastre-Padro, M and Welleweerd, J and Malinen, Eirik and Eilertsen, Karsten and Olsen, Dag and Heide, U. Consequences of leaf calibration errors on IMRT delivery. *Phys Med Biol* **2007**, *52*, 1147–1156.

[21] Wertz, H and Lohr, F and Dobler, B. and Mai, S. and Welzel, G. and Boda-Heggemann, J. and Wenz, F. Dosimetric consequences of a translational isocenter correction based on image guidance for intensity modulated radiotherapy (IMRT) of the prostate. *Phys Med Biol* **2007**, *52*, 5655–5665.

[22] Low, D. and Moran, J. and Dempsey, J. and Dong, L. and Oldham, M. Dosimetry tools and techniques for IMRT. *Med Phys* **2011**, *38*, 1313–1338.

[23] Takahashi, S. Conformation radiotherapy. Rotation techniques as applied to radiography and radiotherapy of cancer. *Acta Radiol Diagn* **1965**, *38*, Suppl 242:1+.

[24] Ahlberg, J.H. and Nilson, E.N. and Walsh, J.L. The theory of splines and their applications. *Canadian Mathematical Bulletin* **1968**, *11*, 507–508.

[25] de Boor, C. A Practical Guide to Spline. In *A Practical Guide to Spline*; Springer; Publishing House: New York, United States of America, 1978.

[26] Chan, T. and Bortfeld, T. and Tsitsiklis, J. A robust approach to IMRT optimization. *Med Phys* **2006**, *33*.

[27] Du, X. and Dang, J. and Wang, Y. and Wang, S. and Lei, T. A Parallel Nonrigid Registration Algorithm Based on B-Spline for Medical Images. *Computational and Mathematical Methods in Medicine* **2016**, *2016.*

[28] Dice, Lee R. Measures of the Amount of Ecologic Association Between Species. *Ecology* **1945**, *26*, 297–302.

[29] Vargas-Bedoya, E. and Rivera, J.C and Sevilla, C. and Puerta, M.E. and Angulo, A. nad Wahl, N. and Cabal, G. Contour Propagation for Radiotherapy Treatment Plans Using Non-Rigid Registration and a Local Search for Parameter Optimization: Study cases in liver and breast. Master-thesis, Universidad EAFIT, Medellín, Colombia, Date of Completion.

[30] Neugebauer, O. *Astronomical cuneiform texts; Babylonian ephemerides of the Seleucid period for the motion of the sun, the moon, and the planets*; London: Published for the Institute for Advanced Study, 1955.

[31] Henry Briggs. Available online: https://www.britannica.com/biography/Henry-Briggs. Accessed 17 July 2022.

[32] Cauchy, A.L. *Cours d'Analyse de l'Ecole royale polytechnique*; L'Imprimerie Royale, Debure frères, Libraires du Roi et de la Bibliothèque du Roi, France, 1821.

[33] Schoenberg, I.J. Contributions to the Problem of Approximation of Equidistant Data by Analytic Functions. In *I. J. Schoenberg Selected Papers*; de Boor, C. Eds.; Birkhäuser Boston: Boston, MA, USA, 1988; pp. 3–57.

[34] Shannon, C. E. Communication in the Presence of Noise. Proceedings of the IRE. *Proc. IRE* **1949**, 37(1), 10–21.

[35] Inglis, A. Review of James Gregory. Tercentenary Memorial Volume. *Math. Gaz.* **1940**, *24*, 125–129.

[36] Siegmund-Schultze, R. Weierstraß's Approximation Theorem (1885) and his 1886 lecture course revisited. In *Karl Weierstraß(1815–1897): Aspekte seines Lebens und Werkes – Aspects of his Life and Work*; König, W., Sprekels, J., Eds.; Springer Fachmedien Wiesbaden: Wiesbaden, Germany, 2016; pp. 219–268.

[37] Birkhoff, G.D. General Mean Value and Remainder Theorems with Applications to Mechanical Differentiation and Quadrature. *AMS* **1906**, *7*, 107–136.

[38] Hou, H. and Andrews, H. Cubic splines for image interpolation and digital filtering. *IEEE Trans Audio Speech Lang Process* **1978**, *26*, 508–517.

[39] Thomas, David H. and Santhanam, Anand and Kishan, Amar U. and Cao, Minsong and Lamb, James and Min, Yugang and O'Connell, Dylan and Yang, Yingli and Agazaryan, Nzhde and Lee, Percy and Low, Daniel. Initial clinical observations of intra- and interfractional motion variation in MR-guided lung SBRT. *BJR* **2018**, *91.*

[40] MatRad. Available online: https://e0404.github.io/matRad/.